pubs.acs.org/Biomac

Article

Tuning Supramolecular Chirality in Iodinated Amphiphilic Peptides Through Tripeptide Linker Editing

Published as part of Biomacromolecules virtual special issue "Peptide Materials".

Douglas S. MacPherson, Dhwanit Dave, Salma Kassem, Selma Doganata, Brian M. Zeglis, and Rein V. Ulijn*

Cite This: *Biomacromolecules* 2024, 25, 2277−2285

Read Online

ACCESS | Metrics & More | Article Recommendations | Supporting Information

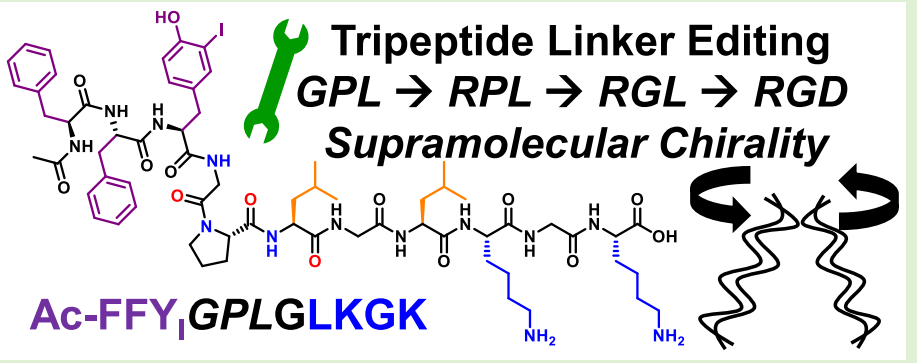

ABSTRACT: Protease-cleavable supramolecular oligopeptide nanofilaments are promising materials for targeted therapeutics and diagnostics. In these systems, single amino acid substitutions can have profound effects on the supramolecular structure and consequent proteolytic degradation, which are critical parameters for their intended applications. Herein, we describe changes to the self-assembly and proteolytic cleavage of iodine containing sequences for future translation into matrix metalloprotease (MMP-9)-activated supramolecular radio-imaging probes. We use a systematic single amino acid exchange in the tripeptide linker region of these peptide amphiphiles to provide insights into the role of each residue in the supramolecular assemblies. These modifications resulted in dramatic changes in the nature of the assembled structures formed, including an unexpected chiral inversion. By using circular dichroism, atomic force microscopy, Fourier transform infrared spectroscopy, and molecular dynamics simulations, we found that the GD loop, a common motif in β-turn elements, induced a reversal of the chiral orientation of the assembled nanofibers. In addition to the impact on peptide packing and chirality, MMP-9-catalyzed hydrolysis was evaluated for the four peptides, with the β-sheet content found to be a stronger determinant of enzymatic hydrolysis than supramolecular chirality. These observations provide fundamental insights into the sequence design in protease cleavable amphiphilic peptides with the potential for radio-labeling and selective biomedical applications.

1. INTRODUCTION

Designed peptide sequences that self-assemble into nanostructures[1−4] continue to receive attention for biomedical applications.[5−8] We are interested in developing matrix metalloprotease (MMP)-activated peptide filaments[9−14] as theranostic agents, which will ultimately involve the direct labeling of peptides with a radioisotope of iodine. The systems are designed to undergo localized, hydrolysis-induced changes in dispersibility catalyzed by target MMPs that are overexpressed by cancer cells, thus giving rise to immobilization or precipitation of the radioisotope at the cancer site, which can function as a therapy or imaging agent. In order to establish a suitable system, we first evaluated peptides with nonradioactive iodotyrosine (Figure 1A). The design builds on previously studied MMP-cleavable peptide sequences[10,11,14] and previously observed differences in assembly and hydrolysis between iodinated and noniodinated peptides, including the unexpected observation of enhanced cleavage kinetics upon iodination.[10] The influence of halogenation in self-assembling peptides has previously been observed in other systems where it has altered peptide self-assembly due to changes in hydrophobicity, H-

Received: October 17, 2023
Revised: January 23, 2024
Accepted: January 23, 2024
Published: March 6, 2024

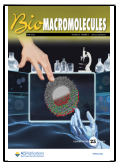

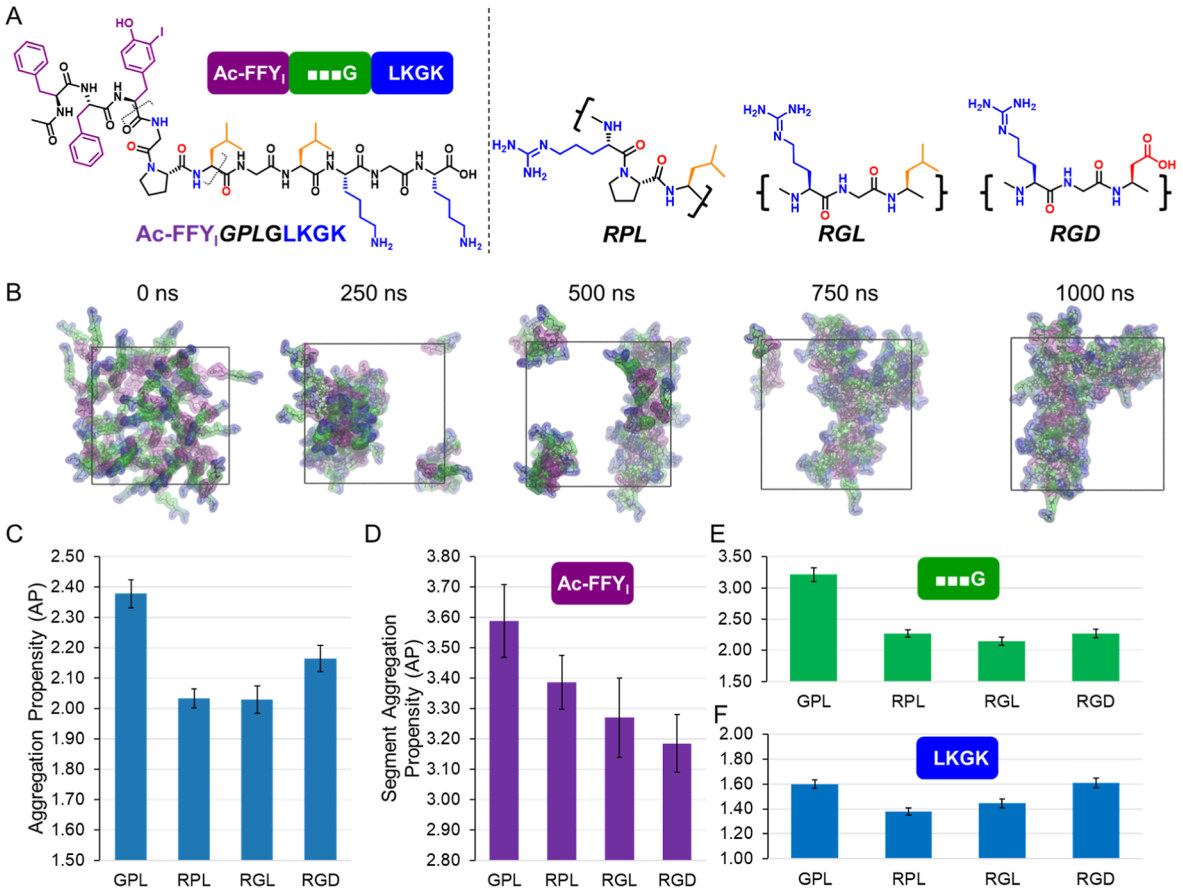

Figure 1. (A) Chemical structures of peptide sequence Ac-FFY$_I$**GPL**GLKGK with identification of hydrophobic peptide segment in purple, the MMP-9 substrate in green and the charged domain in blue, sequence variants exchanging the core sequences of **−RPL−**, **−RGL−**, and **−RGD−**, respectively (right). (B) All-atom MD trajectory snapshots from the self-assembly of 60 **GPL** color coded by the segments showing sequestration of purple segments and solvent exposure of the blue segments. (C) APs for the iodinated tripeptide sequences averaged in the last 100 ns of triplicate self-assembly trajectories. Segmental AP averaged from the last 100 ns of triplicate trajectories for the iodinated peptide segments (D) Ac-FFY$_I$, (E) XXXG tripeptide spacer, and (F) LKGK segment.

bonding, and the introduction of halogen-bonding interactions.[10,15−19]

As previously reported,[10] the iodinated peptide sequence −FY$_I$GPLGLKGK− undergoes rapid and complete hydrolysis by MMP-9. However, both the parent peptide and hydrolysis product formed largely disordered structures rather than the desired micelles and fibers.[10] To overcome this structural disorder, we aimed to tune the peptide sequence in order to favor ordered self-assembly and nanofilament formation. This was achieved through the addition of a second aromatic N-terminal F residue, to enhance self-assembly propensity, and the inclusion of an N-terminal acetyl modification, which has the additional benefit of reducing susceptibility to serum exoprotease activity.[12,20,21] These modifications yielded the sequence Ac-FFY$_I$GPLGLKGK (**GPL**). In addition, we also evaluated the sequence Ac-FFY$_I$**RGD**GLKGK (**RGD**), which incorporates the fibronectin-derived minimally integrin-binding sequence RGD. RGD containing peptides are of interest because integrin controlled cellular attachment influences cell migration, growth, differentiation, and apoptosis, all of which are important factors in the treatment of diseases, such as thrombosis, osteoporosis, and cancer.[22−24] For this latter system, enzymatic hydrolysis would yield Ac-FFY$_I$RGDG, which would not only locally assemble into fibers at the site of MMP activity but also present the RGD sequence for binding to integrins on the cell surface,[25] which are also an attractive target for cancer therapeutics. This would provide a dual-targeting strategy for enhanced localization and residence at cancer sites.[26]

Upon characterization of self-assembled structures formed by **GPL** and **RGD** using circular dichroism (CD), we observed an unexpected inversion of supramolecular chirality (described below). It was hypothesized that such an inversion of supramolecular chirality could have a significant impact on the enzymatic hydrolysis rates, and we therefore included additional single amino acid edit variants of the sequences. This led us to the sequences Ac-FFY$_I$**RPL**GLKGK and Ac-FFY$_I$**RGL**GLKGK (**RPL** and **RGL**) (Figure 1A and Table S1). The focus of the current paper is on understanding the dramatic impact of subtle sequence edits on the peptide's secondary structure, supramolecular chirality, and assembly behavior as an important step in the development of these MMP-responsive theranostic peptide nanostructures Thus, we compared four sequences side-by-side by integrating experimental methods, such as CD, Fourier transform infrared spectroscopy (FTIR), and atomic force microscopy (AFM) microscopy along with computation using atomistic molecular dynamics (MD) to assess the impact of this flexible linker on self-assembly and supramolecular chirality. All-atom MD simulations showed self-assembly for all of the evaluated sequences starting from random configurations. The purple hydrophobic segment underwent rapid sequestra-

https://doi.org/10.1021/acs.biomac.3c01120
Biomacromolecules 2024, 25, 2277−2285

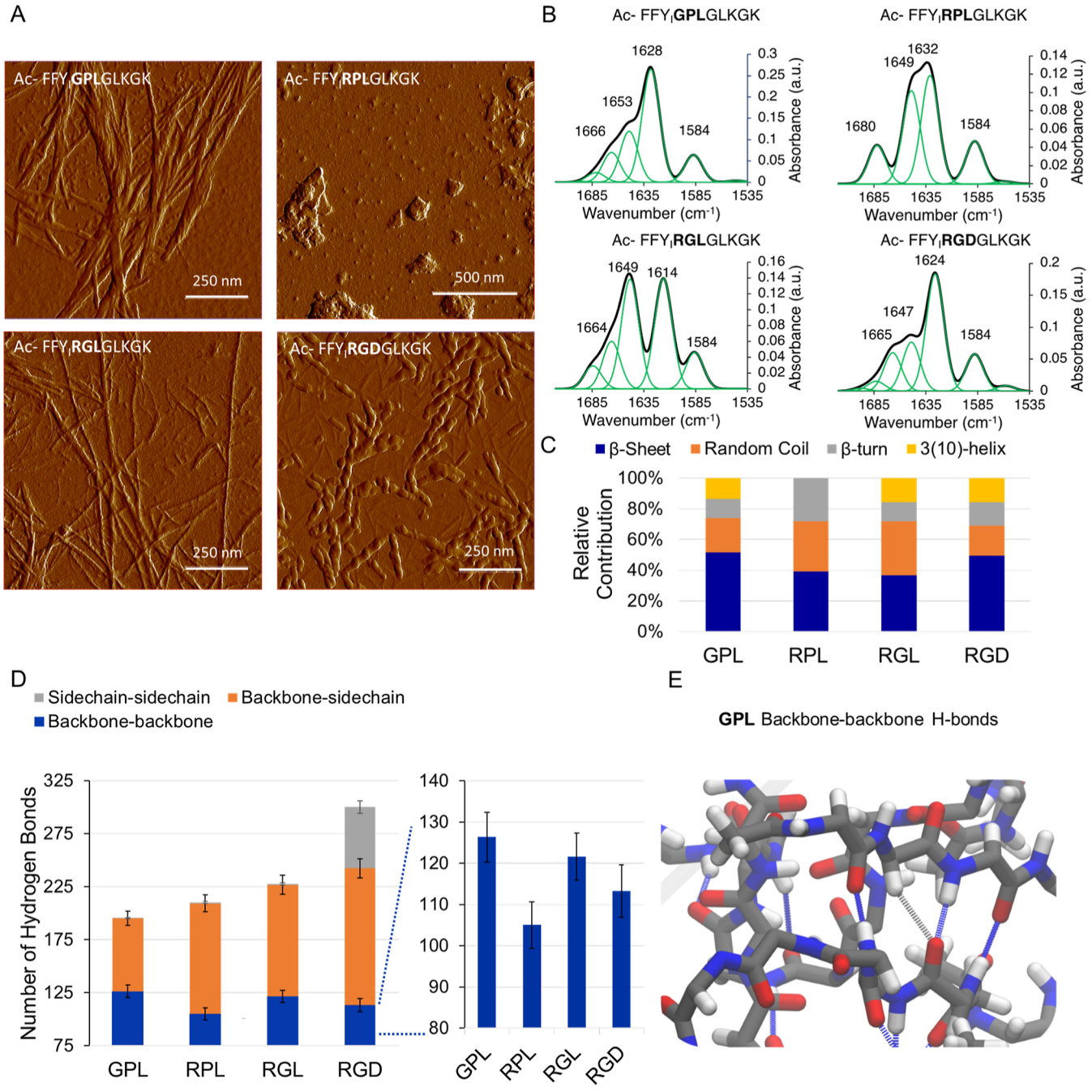

Figure 2. (A) AFM images of **GPL** (top left), **RPL** (top right), **RGL** (bottom left), and **RGD** (bottom right). **GPL** produces bundles of nanofibers, **RPL** assembles into nondistinct aggregates, **RGL** produces nanofibers, and **RGD** assembles into discrete oblong fibers with distinct repeating subunits. 1.0 mM peptide in PBS. (B) FTIR spectra of sequences **GPL**, **RPL**, **RGL**, and **RGD**. Sequence **GPL** shows primarily a β-sheet (1628 cm^{-1}). **RPL** also shows an β-sheet (1632 cm^{-1}) in addition to a random coil (1649 cm^{-1}) and β-turn (1584 cm^{-1}). **RGL** shows dominant contributions from random-coil (1649 cm^{-1}) and β-sheet aggregate (1614 cm^{-1}). **RGD** is primarily the β-sheet (1624 cm^{-1}) with both β-turn and (1584 cm^{-1}) and 3(10)-helix (1665 cm^{-1}). (C) Histogram of the relative contribution of secondary structures derived from FTIR analysis. Percentage values are based on relative peak heights of each structural feature. (D) Analysis of the number of hydrogen bonds between the peptides in the last 100 ns of triplicate trajectories with an inset plot of exclusively backbone−backbone hydrogen bonds between the peptide sequences showing a significantly lower number for **RPL**. (E) Snapshot showing only the backbones of sequence **GPL** interacting via hydrogen bonding.

tion with the blue LKGK end preferring solvent interaction (Figures 1B and S2).

2. EXPERIMENTAL SECTION

2.1. Materials. All peptides were purchased from GenScript with a purity >98% and trifluoroacetyl removed. The samples were dissolved at a concentration of 1.0 mM in 1× phosphate-buffered saline (PBS) supplemented with 1.0 mM $CaCl_2$ and 55 μM $ZnCl_2$ with the pH adjusted to 7.4. Preactivated human recombinant MMP-9 was purchased from Sigma-Aldrich (SKU SAE0078). The enzyme was dissolved in 1× tris buffered saline supplemented with the above $CaCl_2$ and $ZnCl_2$ concentrations and introduced to the peptide at a final concentration of 200 ng/mL.

2.2. Methods. *2.2.1. AFM Analysis.* Samples were prepared by drop-casting 1.0 mM peptide solution in PBS (pH 7.4) onto a mica chip. Samples were allowed to dry for 24 h before being washed 1× with

https://doi.org/10.1021/acs.biomac.3c01120
Biomacromolecules 2024, 25, 2277−2285

deionized H_2O and left to dry for 24 h before imaging. Images were collected on a Bruker Dimension FastScan using a FASTSCAN-B tip on the fast scan mode.

2.2.2. FTIR Analysis. Peptide samples were prepared at a concentration of 10 mM in D_2O and the pH adjusted to 7.4. Sample solution was drop casted between two CaF_2 cells with 12 μm poly(tetrafluoroethylene) spacers. The background was subtracted with D_2O blank alone, and baseline was corrected for the measurement range of interest. Samples were measured on a Bruker Vertex 70 spectrometer with a nitrogen flushed chamber. OPUS software was used to take measurements that were performed at a resolution of 4 cm^{-1}.

2.2.3. CD Analysis. Peptide samples were prepared at a concentration of 0.5 mM for the synthesized cleavage products in 100 μM sodium phosphate buffer pH 7.4. 400 μL of the sample was measured with a 0.1 cm path length quartz cuvette. The background was subtracted with phosphate buffer alone. Samples were measured on a Jasco J-1500 CD spectrophotometer at a range of 300−190 nm at a scanning speed of 100 nm/min. Data is only shown for the measurement range in which the HT values are <800 V.

2.2.4. MD Analysis. All-atom MD simulations-the single peptide molecule in water atomistic boxes were prepared using CHARMM-GUI,[27] where the *N*-acetylation and 3-iodotyrosine modifications were also carried out. The peptide C-termini and Lys (and Arg if present) side chains were ionized. The prepared box configurations had 60 randomly arranged peptide molecules in a $10 \times 10 \times 10$ nm^3 volume. 60 or 120 CL^- ions were added to neutralize this box and TIP3 water molecule for explicit solvent modeling. These boxes were then subjected to steepest descent energy minimization followed by 100 ps *NVT* and *NPT* equilibrations, respectively, using position restraints on the backbone and side chain in order to relax the solvent configuration. Triplicate production MD runs with no restraints were carried out using the CHARMM36 force field for 1000 ns (1 μs) using a 2 fs time step and the leapfrog integrator in GROMACS 2021.7.[28] Structures were saved every 0.1 ns to generate 10,000 frames in each trajectory. LINCS[29] was used to constraint bonds involving hydrogen and the 1.2 nm vdW cutoff was used with a switching distance of 1.0 nm as recommended for the CHARMM36 FF. A Coulomb cutoff of 1.2 nm was used along with Particle Mesh Ewald for long-range electrostatics. Velocity rescale[30] (modified Berendsen-thermostat) and Parrinello−Rahman barostat[31] were used to maintain temperature and pressure coupling to 298 K and 1.0 bar, respectively. Solvent accessible surface areas of the peptides were measured using the *gmx sasa* tool by specifying a solvent probe radius of 0.14 nm. Hydrogen bonds were measured using *gmx hbond* using a distance cutoff and angle cutoff of 0.35 nm and 30°, respectively. Index files were generated to specify the backbone and side-chain atoms to measure pairwise H-bonding (peptide−peptide, backbone−backbone, backbone-side chain, and side chain-side chain). Analyses were carried out using the data from the last 100 ns of the trajectories. Ramachandran angles were measured for each trajectory using *gmx rama* and the residue 5 (P in GPL and **RPL** and G in **RGL** and **RGD**) values from 900 to 1000 ns were used to generate a torsional free energy landscape using *gmx sham* and *gmx xpm2ps*. Trajectories were visualized and rendered using VMD 1.9.3.[32]

2.2.5. Liquid Chromatography—Ultraviolet Light. The reactions were stored at 37 °C, and triplicate samples of the reaction were taken at 0, 24, 48, and 72 h. Liquid chromatography-ultraviolet light (LC-UV) samples were prepared with 15 μL of reaction mixture added to 285 μL 3:1 ratio of MeCN: H_2O + 0.1% formic acid and 0.1 mM caffeine. LC-UV was performed on a Thermo Fisher Exactive Plus LC−MS/UV, with a gradient of MeCN: H_2O + 0.1% formic acid over 8 min through a Phenomenex luna omega 50 × 2.1 mm, 2.1 μm, and 300A C18 column. Xcalibur software was used to quantify the peak area of each chromatogram at 214 nm.

3. RESULTS AND DISCUSSION

3.1. Aggregation Propensity. Using triplicate self-assembly trajectories, we measured the solvent accessible surface area of the peptides and the individual peptide segments (shown in color coded Figure 1A). These were used to compute aggregation propensities (APs) for the overall peptides[33,34] (Figures 1C and S3) as well as for segments (Figures 1D−F and S4) using eqs 1 and 2. All four sequences showed AP scores in the range of 2.00−2.40, indicating that the iodinated amphiphilic peptides underwent self-assembly (Figure 1C). The self-assembly is largely driven by hydrophobic interactions of the N-terminal aromatic residues of the peptides as indicated by the large segment AP scores (>3.00) of the Ac-FFY_I residues, which show some context-dependent trends (Figure 1D). A substantial drop in the AP score was observed for the G to R exchange attributable to the charged side chain of R which is preferentially solvated (Figure 1E). The hydrophilic end of the peptide containing two charged K residues (LKGK) showed segment AP scores closest to 1.00, indicating that the segment maximizes solvent exposure throughout the simulations (Figure 1F).

$$\text{aggregation propensity (AP)} = \frac{\text{SASA}_{\text{initial}}}{\text{SASA}_{\text{time}}} \quad (1)$$

$$\text{segment AP} = \frac{\text{segmental SASA}_{\text{initial}}}{\text{segmental SASA}_{\text{time}}} \quad (2)$$

3.2. AFM Analysis. To experimentally evaluate the self-assembled morphologies, we drop-casted 1.0 mM peptide solutions in PBS buffer (pH 7.4) onto mica chips and dried for 24 h. AFM was used to visualize the nanostructures formed, revealing bundles of extended fibers for **GPL**. For **RPL**, we observed the loss of fiber morphology, with the peptides assembling into indistinct nonfilamentous aggregates of varying sizes from approximately 50−300 nm. In **RGL**, the nanofiber morphology is observed, albeit with less bundling of individual fibers compared to what was observed with the parent **GPL** sequence. Imaging of the **RGD** sequence displays discrete nanofibers of approximately 100−300 nm in length, with a clear visible repeating motif of approximately 50−75 nm that suggests helicity of the fibers (Figures 2A and S9).

3.3. FTIR Spectroscopy. The differences in the morphology observed suggest differences in packing and self-assembly propensity. To evaluate the hydrogen bonding patterns that contribute to the self-assembly of each sequence, and the differences observed between sequences, we performed FTIR analysis.[35] The **GPL** sequence displays a dominant β-sheet peak at 1628 cm^{-1}. A random coil/α-helix contribution is also detectable at 1653 cm^{-1}, in addition to moderate contributions by 3(10)-helix and β-turn signals at 1666 and 1584 cm^{-1}, respectively (Figure 2B,C).[36] Loss of fiber nanostructure results from the replacement of the 4-position G with an R residue in the **RPL** sequence (Figure 2A). Compared to **GPL**, FTIR analysis for **RPL** reveals an increase in the contribution of both the random coil at 1649 cm^{-1} and the 1584 cm^{-1} β-turn feature. The G → R mutation also introduces a distinct band at 1680 cm^{-1} that is also associated with a β-turn motif. Overall, the β-sheet and random coil are the dominant contributors[36] for **RPL** (Figure 2B,C). The sequence **RGL** removes the "helix-breaker" P residue[37] and re-establishes nanofiber morphology (Figure 2A), and we observe two strong peaks at 1649 and 1614 cm^{-1}, indicative of random coil and β-sheet structures, respectively. The 1584 cm^{-1} β-turn is also evident, with the 1664 cm^{-1} 3(10)-helix and 1682 cm^{-1} β-turn also minimally detectable (Figure 2B,C).[36] It is notable that the **RGD** FTIR spectrum is similar to that of **GPL**, with a dominant β-sheet feature at 1624 cm^{-1},

https://doi.org/10.1021/acs.biomac.3c01120
Biomacromolecules 2024, 25, 2277−2285

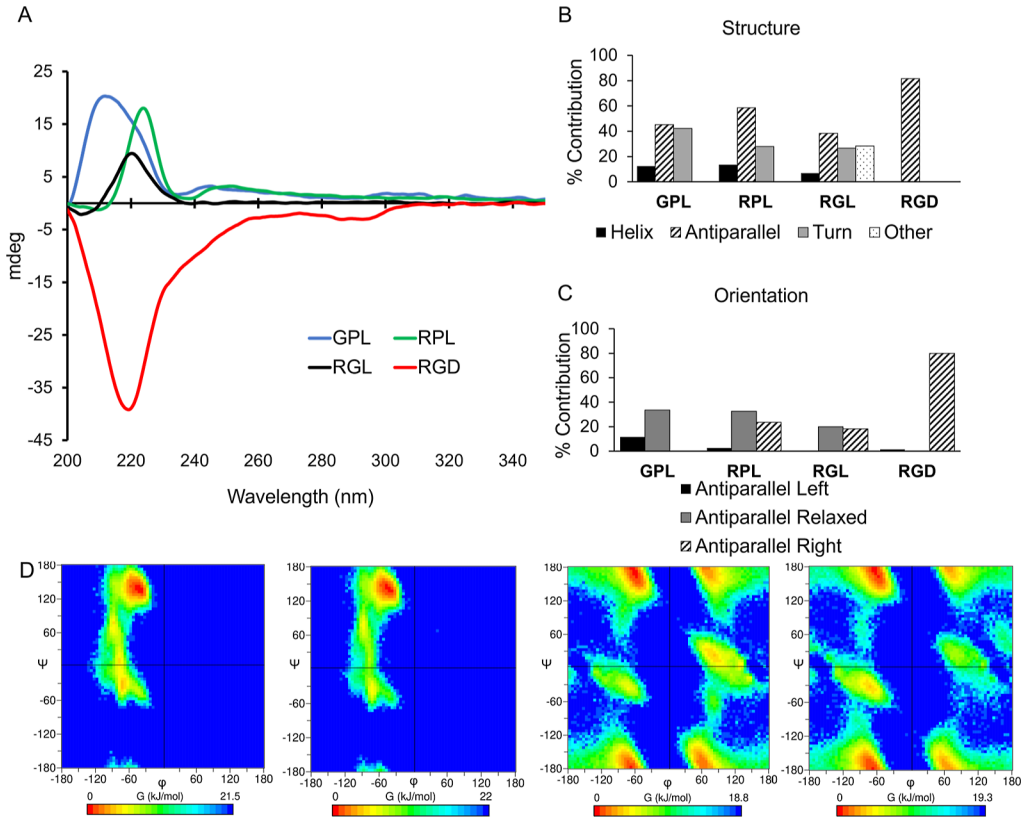

Figure 3. (A) CD spectra of **GPL**, **RPL**, **RGL**, and **RGD** comparing self-assembly and chiral orientation between sequences at 0.5 mM in 100 μM sodium phosphate buffer. (B) Percentage of estimated underlying secondary structure formed by peptide self-assembly revealed through deconvolution of CD spectra provided by BeStSel fitting algorithm. (C) Percentage of estimated orientation of antiparallel contributions revealed through deconvolution of CD spectra provided by BeStSel fitting algorithm. (D) Ramachandran free energy landscapes for Pro (residue 5) in **GPL**, **RPL**, and for Gly (residue 5) in **RGL** and **RGD** from the last 100 ns of three independent trajectories.

along with the β-turn and random coil features found at 1584 and 1647 cm^{-1}, respectively. However, **RGD** features a more prominent 1665 cm^{-1} 3(10)-helix feature compared to **GPL** and the other variants (Figure 2B,C).[36] The β-sheet content was found to be higher for **GPL** and **RGD** with a lower corresponding absorbance observed for **RPL** and **RGL** (Figure 2B,C).

3.4. Hydrogen Bonding Analyses. To investigate the influence of these single amino acid exchanges on the hydrogen bonding patterns of these iodinated peptide amphiphiles, as observed by FTIR, we revisited the all-atom MD simulations with explicit solvents. From triplicate 1 μs trajectories of the tested sequences, we used the equilibrated last 100 ns for statistical averages of hydrogen bonding (Figures 2D and S5–S8). Interestingly, the total number of hydrogen bonds (Figures 2D and S5) formed between the 60 peptide molecules simulated does not covary with the AP score trend (Figure 1C) showing an increasing trend in the following order **GPL** < **RPL** < **RGL** ≪ **RGD**. We decomposed the total number of hydrogen bonds into contributions arising from backbone−backbone (Figures 2D and S6), backbone-side-chain (Figures 2D and S7), and side chain-side chain (Figures 2D and S8) interactions. Backbone−backbone H-bonds are indicative of directional assemblies stabilized by β-sheet-like H-bonding topologies (Figure 2E) and in excellent agreement with experimental observations; we find that the **RPL** sequence shows the lowest number of these H-bonds (Figures 2D and S6), explaining the loss of extended 1D self-assembled structures observed in the AFM (Figure 2A). P in the backbone can disrupt packing by steric changes while additionally removing the NH donor on the backbone. These structural changes of P along with the preferred solvation and electrostatic repulsion of the R side chain in **RPL** could be a probable cause for the disruption of isotropic self-assembly. Changing P to G in **RGL** appears to restore the backbone−backbone H-bonds by enabling conformational flexibility to assemble in an anisotropic H-bonding topology (Figure 2D). Complementary electrostatics drives H-bonding between R−D and K−D in **RGD** leading to a large contribution of side chain-side chain H-bonds relative to the other sequences (Figures 2D and S8).

3.5. Circular Dichroism. Supramolecular organization within the peptide assemblies was further evaluated by CD. The CD spectrum of **GPL** features a prominent peak at 215 nm (Figures 3A and S1), typical for peptide β-sheet structures.[38,39] For **RPL**, a sharper peak is observed with a slight red shift to 225 nm. A smaller peak at 250 nm also contributes, which has been associated with the helical arrangement of aromatic groups (Figure 3A).[40] The key features of the spectrum observed for **RGL** resemble that of **GPL** and **RPL**, with well-defined peaks at 221 nm; however, there is no contribution observed in the 250 nm range, suggesting reduced chiral structuring of the aromatic regions (Figure 3A). In notable contrast to the other three sequences and unexpectedly, the CD spectrum for **RGD** is inverted at the x-axis, indicating a switching of supramolecular chirality. The **RGD** minima occurs at 220 nm, which is associated with both β-sheets and superhelical arrangements.[39,41,42] A smaller feature at 290 nm (Figure 3A) could be associated with aromatic stacking.[15,40] Deconvolution of the

https://doi.org/10.1021/acs.biomac.3c01120
Biomacromolecules 2024, 25, 2277−2285

CD spectra using BeStSel[43] fitting algorithm illuminates the underlying structures formed by the self-assembling peptides and allows a comparison with the FTIR results. **GPL** displays a mixture of antiparallel and turn conformations, with some helical structures as well. **RPL** has similar characteristics, with a more antiparallel contribution. **RGL** has a significant undefined structure, in agreement with the FTIR data. Remarkably, **RGD** displays only an antiparallel structure (Figure 3B). Further analysis of the antiparallel orientation of each peptide shows mostly relaxed structures for **GPL** with some "left" contributions. **RPL** and **RGL** both show a mixture of relaxed structure and "right" orientation, and **RGD** shows a dominant "right" antiparallel orientation (Figure 3C).

The inverted supramolecular chirality observed in the **RGD** sequence suggests that the aspartic acid (D) residue is a critical feature contributing to the chiral switch. Indeed, "GD" is often found in β-turns that connect the strands of antiparallel β-hairpins, e.g., with turns between α-helices having preferences for D residues within the turns,[44] including alpha-left-beta ($\alpha_L\beta$) turns containing GD within a helical structure.[44,45] Alva et al. identified a feature they term as "GD box", which is featured in two unpaired β-strands connected by a β-turn. In an analysis of resolved protein structures containing the GD box, the element is frequently found in β-turn motifs and have been identified as a supersecondary structure element.[46] We believe the presence of the GD residues in our **RGD** peptide contributes to this change in supramolecular chirality and, therefore, we used our all-atom MD trajectories to compute the torsional free energy landscape around the residues P (residue 5) in **GPL** and **RPL** and G (residue 5) in **RGL** and **RGD** (Figure 3D). The cyclized side chain and consequently conformationally restricted nature of P constraints the sampled Ramachandran dihedral angles largely to the domains associated with the ppII helix for both **GPL** and **RPL**.[47] Sampling of the P α region appears to be more prevalent for **GPL**, indicating that having a flexible neighboring residue (G) at position 4, imparts some conformational flexibility. For the G free energy landscape, due to the achiral and nonbulky nature of the side chain, all four Ramachandran quadrants are sampled in the case of **RGL**. Surprisingly, upon mutation of L to D in position 6 (**RGD**), the G dihedrals appear to sample the two left-quadrants of the Ramachandran free energy landscape, and this is indicative of a right-handed chiral predisposition. This change in the sampling of chiral structures agrees with the observation of inversion of the CD signal in Figure 3A as well as the orientational preference in Figure 3C for **RGD**.

3.6. Sequence Evaluation. Combining insights from MD and structure characterization, we examined the systematic amino-acid variation in the central tripeptide spacer residues was examined. For **GPL**, the core sequence is abundant in the collagen triple helix,[48] followed by leucine (L), often found in helical structural motifs.[49] For **RPL**, The G → R edit introduces a positively charged side chain, capable of participating in electrostatic interactions, salt bridges, and multiple hydrogen bonds, disrupting fiber formation (Figure 2A). CD analysis elucidates that the neighboring residue of the P[50] toward the N-terminal direction plays a key role in disrupting the self-assembly (Figure 2A) as well as preferred torsional sampling (Figure 3D) for the rigid cyclic amino acid in the **GPL** and **RPL** sequences.

G mutation allows for longer range of self-assembly, whereas R encourages only short-range order (Figure 2A), as supported by the backbone−backbone H-bonds (Figure 2D). On the other hand, the use of the flexible central residue of G in **RGL** and **RGD** tripeptide spacers restores self-assembly propensities (Figure 2A,D). The **RGL** sequence contains the positively charged R, followed by a reintroduction of G and L. The P is removed, making the peptide more flexible and likely permitting the R to participate in more bonding interactions. We note that the **RGD** sequence is composed of the positively charged R residue followed by G and finally negatively charged aspartic acid (D). This is the only sequence that includes a positive and negative charge separated by the conformationally flexible G.[51] As evidenced by the torsional landscape around the G in RGD, a conformational turn is induced, which may be supported by the increase in relative contribution of the 3(10)-helix revealed by the FTIR analysis (Figure 2B,C). Surprisingly, D side chain influences the chirality of the self-assembly in a strikingly different fashion compared to L with an inversion of the cotton effect in CD, changes in side chain-side chain H-bonding as well as preferred torsional sampling for the G (Figures 2A,D and 3A,D).

3.7. MMP-Catalyzed Hydrolysis of Peptide Nanofibers. We were interested in evaluating whether chirality or secondary structure would influence the rate and extent of peptide hydrolysis by MMP-9. For this evaluation, the four peptides were exposed to MMP-9 activated by 4-aminophenylmercuric acetate and triplicate samples of the reaction were taken at 0 (no enzyme added) 24, 48, and 72 h and analyzed by LC-UV. By 72 h, **GPL** underwent 14% (±0.4%) hydrolysis, slightly exceeding that of **RPL** 11.0% (±1.7%). **RGL** underwent the most hydrolysis with 29.2% (±1.1%) due to the preferred action of MMP-9 between the G and L residues. Similar to **GPL** and **RPL**, the **RGD** sequence underwent 14.9% (±1.5%) hydrolysis by 72 h (Figure 4A). These observations indicate that the substitution

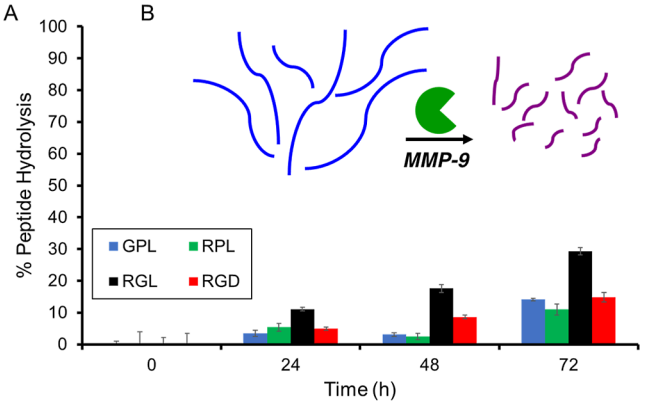

Figure 4. Peptide hydrolysis compared to degree of order in the self-assembled peptide structures. (A) MMP-9-catalyzed peptide hydrolysis over time for **GPL**, **RPL**, **RGL**, and **RGD** (1.0 mM peptide + 200 ng/mL MMP-9) measured in triplicate using quantitative LC-UV over 72 h. (B) Schematic showing the action of MMP-9 on the amphiphilic peptide nanostructures.

of the 5-position P with a G, and the increased contribution of random coil secondary structure permits better access to the peptides by MMP-9 and thus more complete hydrolysis (Figure 4B). In contrast to the sequences presented in a previous work,[10] none of the four peptides evaluated here underwent complete hydrolysis by the enzyme. Compared to the sequence $FY_IGPLGLKGK$, which underwent compete hydrolysis by 12 h,[10] the sequence Ac-$FFY_IGPLGLKGK$, which contains the same core MMP-responsive sequence, is effectively impervious to degradation by MMP-9 (Figure 4A). This is likely due to the rigid amyloid-like β-sheets stabilized by the second F residue

https://doi.org/10.1021/acs.biomac.3c01120
Biomacromolecules 2024, 25, 2277−2285

and the N-terminal acetyl group, effectively limiting access to the individual peptide substrates.

4. CONCLUSIONS

Packing and related balance of order and disorder and supramolecular chirality[52−54] within peptide nanostructures is strongly dictated by the peptide sequence.[10,11,14,55] We found that the tripeptide linker in these amphiphilic-iodinated sequences can play a key role in influencing self-assembly, long-range order, and supramolecular chirality.

We found that the three-residue modification "**RGD**" in the central region of the evaluated nanofilament-forming-iodinated sequence induced a chiral inversion. In certain biomedical contexts, peptide nanostructures are likely to be degraded by proteases, and sequence design may be exploited to enhance degradation by specific (disease-related) proteases, including MMP enzymes. MMPs are overexpressed in some metastatic cancers and have been explored as targets and activators for diagnostics and therapy.[56−58] The observed proteolytic activity is dependent not only on peptide sequence recognition but also on enzyme access through charge, packing, and strength of interaction between peptide molecules within supramolecular structures,[10,14,59] which may be further impacted by inclusion of payload molecules.[11]

To our knowledge, this is the first report of an MMP-responsive peptide that combines the introduction of iodine (for future radioactive labeling) with fibrillar assemblies. Based on the sequences evaluated, these results indicate that the chiral switching resulting from the amino acid substitution does not significantly change the hydrolysis by MMP-9. MMP-9 is substrate-specific, and slight peptide sequence variations can change the rate and extent of peptide hydrolysis by MMP-9.[14] We observe that tightly packed self-assembled peptides do not undergo extensive enzymatic hydrolysis compared with those that provide a more accessible substrate for the enzyme. These findings provide us with useful insights into the design of self-assembling and enzyme responsive sequences. Sequence design to balance order and disorder and thus enzyme response provides a further set of design rules for the development of translatable clinically useful enzyme-responsive peptides.

■ ASSOCIATED CONTENT

Supporting Information

The Supporting Information is available free of charge at https://pubs.acs.org/doi/10.1021/acs.biomac.3c01120.

MS data, CD spectra at 0.25 mM for GPL and RGD, snapshots from MD trajectories of RPL, RGL, and RGD, total and segmental aggregation propensities (APs) time evolution plots, and hydrogen bonding analyses from MD trajectories (PDF)

■ AUTHOR INFORMATION

Corresponding Author

Rein V. Ulijn − *Advanced Science Research Center (ASRC) at The Graduate Center, City University of New York, New York, New York 10031, United States; Department of Chemistry, Hunter College of the City University of New York, New York, New York 10028, United States; Ph.D. Program in Biochemistry and Ph.D. Program in Chemistry, The Graduate Center of the City University of New York, New York, New York 10016, United States;* orcid.org/0000-0002-7138-1213; Email: RUlijn@gc.cuny.edu

Authors

Douglas S. MacPherson − *Advanced Science Research Center (ASRC) at The Graduate Center, City University of New York, New York, New York 10031, United States; Department of Chemistry, Hunter College of the City University of New York, New York, New York 10028, United States; Ph.D. Program in Biochemistry, The Graduate Center of the City University of New York, New York, New York 10016, United States; Department of Radiology, Memorial Sloan Kettering Cancer Center, New York, New York 10065, United States*

Dhwanit Dave − *Advanced Science Research Center (ASRC) at The Graduate Center, City University of New York, New York, New York 10031, United States; Department of Chemistry, Hunter College of the City University of New York, New York, New York 10028, United States; Ph.D. Program in Chemistry, The Graduate Center of the City University of New York, New York, New York 10016, United States;* orcid.org/0000-0002-6218-4584

Salma Kassem − *Advanced Science Research Center (ASRC) at The Graduate Center, City University of New York, New York, New York 10031, United States*

Selma Doganata − *Advanced Science Research Center (ASRC) at The Graduate Center, City University of New York, New York, New York 10031, United States; Macaulay Honors College, City University of New York, New York, New York 10031, United States*

Brian M. Zeglis − *Department of Chemistry, Hunter College of the City University of New York, New York, New York 10028, United States; Ph.D. Program in Biochemistry and Ph.D. Program in Chemistry, The Graduate Center of the City University of New York, New York, New York 10016, United States; Department of Radiology, Memorial Sloan Kettering Cancer Center, New York, New York 10065, United States; Department of Radiology, Weill Cornell Medical College, New York, New York 10065, United States;* orcid.org/0000-0002-9091-744X

Complete contact information is available at: https://pubs.acs.org/10.1021/acs.biomac.3c01120

Author Contributions

○D.S.M. and D.D. contributed equally to this paper. The manuscript was written through contributions of all authors. All authors have given approval to the final version of the manuscript.

Funding

This work is partially supported by the National Science Foundation CREST Center for Interface Design and Engineered Assembly of Low Dimensional systems (IDEALS), NSF grant number HRD-1547830 the R.V.U. acknowledges funding from Office of Naval Research for the Vannevar Bush Faculty Fellowship (grant N00014-21-1-2967), D.D. and R.V.U. acknowledge U.S. Air Force Office of Scientific Research (grant FA9550-19-1-0111).

Notes

The authors declare no competing financial interest.

■ ACKNOWLEDGMENTS

The authors are thankful to H. Christopher Fry for his advice concerning GD box contribution to structural turns.

■ ABBREVIATIONS

MMP, matrix metalloprotease; CD, circular dichroism; AFM, atomic force microscopy; FTIR, Fourier transform infrared spectroscopy

■ REFERENCES

(1) Hamley, I. W. Peptides for Vaccine Development. *ACS Appl. Bio Mater.* **2022**, *5* (3), 905−944.
(2) Ulijn, R. V.; Smith, A. M. Designing Peptide Based Nanomaterials. *Chem. Soc. Rev.* **2008**, *37* (4), 664−675.
(3) Sato, K.; Hendricks, M. P.; Palmer, L. C.; Stupp, S. I. Peptide Supramolecular Materials for Therapeutics. *Chem. Soc. Rev.* **2018**, *47* (20), 7539−7551.
(4) Levin, A.; Hakala, T. A.; Schnaider, L.; Bernardes, G. J. L.; Gazit, E.; Knowles, T. P. J. Biomimetic Peptide Self-Assembly for Functional Materials. *Nat. Rev. Chem.* **2020**, *4* (11), 615−634.
(5) Zhang, S. Fabrication of Novel Biomaterials through Molecular Self-Assembly. *Nat. Biotechnol.* **2003**, *21* (10), 1171−1178.
(6) Cui, H.; Webber, M. J.; Stupp, S. I. Self-Assembly of Peptide Amphiphiles: From Molecules to Nanostructures to Biomaterials. *Pept. Sci.* **2010**, *94* (1), 1−18.
(7) Wang, J.; Li, Y.; Nie, G. Multifunctional Biomolecule Nanostructures for Cancer Therapy. *Nat. Rev. Mater.* **2021**, *6* (9), 766−783.
(8) Lopez-Silva, T. L.; Schneider, J. P. From Structure to Application: Progress and Opportunities in Peptide Materials Development. *Curr. Opin. Chem. Biol.* **2021**, *64*, 131−144.
(9) Son, J.; Parveen, S.; MacPherson, D.; Marciano, Y.; Huang, R. H.; Ulijn, R. V. MMP-Responsive Nanomaterials. *Biomater. Sci.* **2023**, *11*, 6457−6479.
(10) Macpherson, D. S.; McPhee, S. A.; Zeglis, B. M.; Ulijn, R. V. The Impact of Tyrosine Iodination on the Aggregation and Cleavage Kinetics of MMP-9-Responsive Peptide Sequences. *ACS Biomater. Sci. Eng.* **2022**, *8* (2), 579−587.
(11) Marciano, Y.; Del Solar, V.; Nayeem, N.; Dave, D.; Son, J.; Contel, M.; Ulijn, R. V. Encapsulation of Gold-Based Anticancer Agents in Protease-Degradable Peptide Nanofilaments Enhances Their Potency. *J. Am. Chem. Soc.* **2023**, *145* (1), 234−246.
(12) Marciano, Y.; Nayeem, N.; Dave, D.; Ulijn, R. V.; Contel, M. N-Acetylation of Biodegradable Supramolecular Peptide Nanofilaments Selectively Enhances Their Proteolytic Stability for Targeted Delivery of Gold-Based Anticancer Agents. *ACS Biomater. Sci. Eng.* **2023**, *9* (6), 3379−3389.
(13) Li, Y.; Yang, G.; Gerstweiler, L.; Thang, S. H.; Zhao, C.-X. Design of Stimuli-Responsive Peptides and Proteins. *Adv. Funct. Mater.* **2023**, *33* (7), 2210387.
(14) Son, J.; Kalafatovic, D.; Kumar, M.; Yoo, B.; Cornejo, M. A.; Contel, M.; Ulijn, R. V. Customizing Morphology, Size, and Response Kinetics of Matrix Metalloproteinase-Responsive Nanostructures by Systematic Peptide Design. *ACS Nano* **2019**, *13* (2), 1555−1562.
(15) Ryan, D. M.; Anderson, S. B.; Nilsson, B. L. The Influence of Side-Chain Halogenation on the Self-Assembly and Hydrogelation of Fmoc-Phenylalanine Derivatives. *Soft Matter* **2010**, *6* (14), 3220−3231.
(16) Bertolani, A.; Pirrie, L.; Stefan, L.; Houbenov, N.; Haataja, J. S.; Catalano, L.; Terraneo, G.; Giancane, G.; Valli, L.; Milani, R.; Ikkala, O.; Resnati, G.; Metrangolo, P. Supramolecular Amplification of Amyloid Self-Assembly by Iodination. *Nat. Commun.* **2015**, *6* (1), 7574.
(17) Sloand, J. N.; Culp, T. E.; Wonderling, N. M.; Gomez, E. D.; Medina, S. H. Mechanomorphogenic Films Formed via Interfacial Assembly of Fluorinated Amino Acids. *Adv. Funct. Mater.* **2021**, *31* (40), 2104223.
(18) Pizzi, A.; Sori, L.; Pigliacelli, C.; Gautieri, A.; Andolina, C.; Bergamaschi, G.; Gori, A.; Panine, P.; Grande, A. M.; Linder, M. B.; Baldelli Bombelli, F.; Soncini, M.; Metrangolo, P. Emergence of Elastic Properties in a Minimalist Resilin-Derived Heptapeptide upon Bromination. *Small* **2022**, *18* (32), 2200807.
(19) Li, D.; Ma, Y.; Xia, W.; Tao, Y.; Zhang, Y.; Zhang, H.; Li, D.; Dai, B.; Liu, C. Creating an Amyloid 'Kaleidoscope' Using Short Iodinated Peptides. *Angew. Chem.* **2023**, *135* (42), No. e202310737.
(20) Pei, J.; Gao, X.; Pan, D.; Hua, Y.; He, J.; Liu, Z.; Dang, Y. Advances in the Stability Challenges of Bioactive Peptides and Improvement Strategies. *Curr. Res. Food Sci.* **2022**, *5*, 2162−2170.
(21) Benuck, M.; Marks, N. Differences in the Degradation of Hypothalamic Releasing Factors by Rat and Human Serum. *Life Sci.* **1976**, *19* (8), 1271−1276.
(22) Hersel, U.; Dahmen, C.; Kessler, H. RGD Modified Polymers: Biomaterials for Stimulated Cell Adhesion and Beyond. *Biomaterials* **2003**, *24* (24), 4385−4415.
(23) Pierschbacher, M. D.; Ruoslahti, E. Cell Attachment Activity of Fibronectin Can Be Duplicated by Small Synthetic Fragments of the Molecule. *Nature* **1984**, *309* (5963), 30−33.
(24) Alipour, M.; Baneshi, M.; Hosseinkhani, S.; Mahmoudi, R.; Jabari Arabzadeh, A.; Akrami, M.; Mehrzad, J.; Bardania, H. Recent Progress in Biomedical Applications of RGD-Based Ligand: From Precise Cancer Theranostics to Biomaterial Engineering: A Systematic Review. *J. Biomed. Mater. Res. A* **2020**, *108* (4), 839−850.
(25) Desgrosellier, J. S.; Cheresh, D. A. Integrins in Cancer: Biological Implications and Therapeutic Opportunities. *Nat. Rev. Cancer* **2010**, *10* (1), 9−22.
(26) Ruoslahti, E. RGD and Other Recognition Sequences for Integrins. *Annu. Rev. Cell Dev. Biol.* **1996**, *12*, 697−715.
(27) Jo, S.; Kim, T.; Iyer, V. G.; Im, W. CHARMM-GUI: A Web-Based Graphical User Interface for CHARMM. *J. Comput. Chem.* **2008**, *29* (11), 1859−1865.
(28) Abraham, M. J.; Murtola, T.; Schulz, R.; Páll, S.; Smith, J. C.; Hess, B.; Lindahl, E. GROMACS: High Performance Molecular Simulations through Multi-Level Parallelism from Laptops to Supercomputers. *SoftwareX* **2015**, *1−2*, 19−25.
(29) Hess, B. P-LINCS: A Parallel Linear Constraint Solver for Molecular Simulation. *J. Chem. Theory Comput.* **2008**, *4* (1), 116−122.
(30) Bussi, G.; Donadio, D.; Parrinello, M. Canonical Sampling through Velocity Rescaling. *J. Chem. Phys.* **2007**, *126* (1), 014101.
(31) Parrinello, M.; Rahman, A. Polymorphic Transitions in Single Crystals: A New Molecular Dynamics Method. *J. Appl. Phys.* **1981**, *52* (12), 7182−7190.
(32) Humphrey, W.; Dalke, A.; Schulten, K. VMD: Visual Molecular Dynamics. *J. Mol. Graphics* **1996**, *14* (1), 33−38.
(33) Frederix, P. W. J. M.; Ulijn, R. V.; Hunt, N. T.; Tuttle, T. Virtual Screening for Dipeptide Aggregation: Toward Predictive Tools for Peptide Self-Assembly. *J. Phys. Chem. Lett.* **2011**, *2* (19), 2380−2384.
(34) Ramakrishnan, M.; van Teijlingen, A.; Tuttle, T.; Ulijn, R. V. Integrating Computation, Experiment, and Machine Learning in the Design of Peptide-Based Supramolecular Materials and Systems. *Angew. Chem., Int. Ed.* **2023**, *62* (18), No. e202218067.
(35) Kong, J.; Yu, S. Fourier Transform Infrared Spectroscopic Analysis of Protein Secondary Structures. *Acta Biochim. Biophys. Sin.* **2007**, *39* (8), 549−559.
(36) Cobb, J. S.; Zai-Rose, V.; Correia, J. J.; Janorkar, A. V. FT-IR Spectroscopic Analysis of the Secondary Structures Present during the Desiccation Induced Aggregation of Elastin-Like Polypeptide on Silica. *ACS Omega* **2020**, *5* (14), 8403−8413.
(37) Imai, K.; Mitaku, S. Mechanisms of Secondary Structure Breakers in Soluble Proteins. *Biophysics* **2005**, *1*, 55−65.
(38) Aggeli, A.; Nyrkova, I. A.; Bell, M.; Harding, R.; Carrick, L.; McLeish, T. C. B.; Semenov, A. N.; Boden, N. Hierarchical self-assembly of chiral rod-like molecules as a model for peptide β-sheet tapes, ribbons, fibrils, and fibers. *Proc. Natl. Acad. Sci.* **2001**, *98* (21), 11857−11862.
(39) Smith, A. M.; Williams, R. J.; Tang, C.; Coppo, P.; Collins, R. F.; Turner, M. L.; Saiani, A.; Ulijn, R. V. Fmoc-Diphenylalanine Self Assembles to a Hydrogel via a Novel Architecture Based on $\pi-\pi$ Interlocked β-Sheets. *Adv. Mater.* **2008**, *20* (1), 37−41.
(40) Yang, Z.; Gu, H.; Fu, D.; Gao, P.; Lam, J. K.; Xu, B. Enzymatic Formation of Supramolecular Hydrogels. *Adv. Mater.* **2004**, *16* (16), 1440−1444.

https://doi.org/10.1021/acs.biomac.3c01120
Biomacromolecules 2024, 25, 2277−2285

(41) Qi, P.; Zhou, Y.; Wang, D.; He, Z.; Li, Z. A New Collagen Solution with High Concentration and Collagen Native Structure Perfectly Preserved. *RSC Adv.* **2015**, *5* (106), 87180−87186.
(42) Jayawarna, V.; Smith, A.; Gough, J. E.; Ulijn, R. V. Three-Dimensional Cell Culture of Chondrocytes on Modified Di-Phenylalanine Scaffolds. *Biochem. Soc. Trans.* **2007**, *35* (3), 535−537.
(43) Micsonai, A.; Moussong, E.; Wien, F.; Boros, E.; Vadászi, H.; Murvai, N.; Lee, Y. H.; Molnár, T.; Réfrégiers, M.; Goto, Y.; Tantos, A.; Kardos, J. BeStSel: Web server for Secondary Structure and Fold Prediction for Protein CD Spectroscopy. *Nucleic Acids Res.* **2022**, *50* (W1), W90−W98.
(44) Lahr, S. J.; Engel, D. E.; Stayrook, S. E.; Maglio, O.; North, B.; Geremia, S.; Lombardi, A.; DeGrado, W. F. Analysis and Design of Turns in α-Helical Hairpins. *J. Mol. Biol.* **2005**, *346* (5), 1441−1454.
(45) Fry, H. C.; Lehmann, A.; Sinks, L. E.; Asselberghs, I.; Tronin, A.; Krishnan, V.; Blasie, J. K.; Clays, K.; Degrado, W. F.; Saven, J. G.; Therien, M. J. Computational de Novo Design and Characterization of a Protein That Selectively Binds a Highly Hyperpolarizable Abiological Chromophore. *J. Am. Chem. Soc.* **2013**, *135* (37), 13914−13926.
(46) Alva, V.; Dunin-Horkawicz, S.; Habeck, M.; Coles, M.; Lupas, A. N. The GD Box: A Widespread Noncontiguous Supersecondary Structural Element. *Protein Sci.* **2009**, *18* (9), 1961−1966.
(47) Horng, J.-C.; Raines, R. T. Stereoelectronic Effects on Polyproline Conformation. *Protein Sci.* **2006**, *15* (1), 74−83.
(48) de Paz-Lugo, P.; Lupiáñez, J. A.; Meléndez-Hevia, E. High Glycine Concentration Increases Collagen Synthesis by Articular Chondrocytes in Vitro: Acute Glycine Deficiency Could Be an Important Cause of Osteoarthritis. *Amino Acids* **2018**, *50* (10), 1357−1365.
(49) Landschulz, W. H.; Johnson, P. F.; McKnight, S. L. The Leucine Zipper: A Hypothetical Structure Common to a New Class of DNA Binding Proteins. *Science* **1988**, *240* (4860), 1759−1764.
(50) Li, S. C.; Goto, N. K.; Williams, K. A.; Deber, C. M. Alpha-Helical, but Not Beta-Sheet, Propensity of Proline Is Determined by Peptide Environment. *Proc. Natl. Acad. Sci.* **1996**, *93* (13), 6676−6681.
(51) Huang, F.; Nau, W. M. A Conformational Flexibility Scale for Amino Acids in Peptides. *Angew. Chem., Int. Ed.* **2003**, *42* (20), 2269−2272.
(52) Lee, H. E.; Ahn, H. Y.; Lee, J.; Nam, K. T. Biomolecule-Enabled Chiral Assembly of Plasmonic Nanostructures. *ChemNanoMat* **2017**, *3* (10), 685−697.
(53) Coppage, R.; Slocik, J. M.; Briggs, B. D.; Frenkel, A. I.; Naik, R. R.; Knecht, M. R. Determining Peptide Sequence Effects That Control the Size, Structure, and Function of Nanoparticles. *ACS Nano* **2012**, *6* (2), 1625−1636.
(54) Saiani, A.; Mohammed, A.; Frielinghaus, H.; Collins, R.; Hodson, N.; Kielty, C. M.; Sherratt, M. J.; Miller, A. F. Self-assembly and gelation properties of α-helix versus β-sheet forming peptides. *Soft Matter* **2009**, *5* (1), 193−202.
(55) Ulijn, R. V.; Lampel, A. Order/Disorder in Protein and Peptide-Based Biomaterials. *Isr. J. Chem.* **2020**, *60* (12), 1129−1140.
(56) Gialeli, C.; Theocharis, A. D.; Karamanos, N. K. Roles of Matrix Metalloproteinases in Cancer Progression and Their Pharmacological Targeting. *FEBS J.* **2011**, *278* (1), 16−27.
(57) Olson, E. S.; Jiang, T.; Aguilera, T. A.; Nguyen, Q. T.; Ellies, L. G.; Scadeng, M.; Tsien, R. Y. Activatable Cell Penetrating Peptides Linked to Nanoparticles as Dual Probes for in Vivo Fluorescence and MR Imaging of Proteases. *Proc. Natl. Acad. Sci.* **2010**, *107* (9), 4311−4316.
(58) Battistella, C.; Callmann, C. E.; Thompson, M. P.; Yao, S.; Yeldandi, A. V.; Hayashi, T.; Carson, D. A.; Gianneschi, N. C. Delivery of Immunotherapeutic Nanoparticles to Tumors via Enzyme-Directed Assembly. *Adv. Healthcare Mater.* **2019**, *8* (23), 1901105.
(59) Debnath, S.; Roy, S.; Abul-Haija, Y. M.; Frederix, P. W. J. M.; Ramalhete, S. M.; Hirst, A. R.; Javid, N.; Hunt, N. T.; Kelly, S. M.; Angulo, J.; Khimyak, Y. Z.; Ulijn, R. V. Tunable Supramolecular Gel Properties by Varying Thermal History. *Chem. Eur. J.* **2019**, *25* (33), 7881−7887.

https://doi.org/10.1021/acs.biomac.3c01120
Biomacromolecules 2024, 25, 2277−2285